

Response of a Flat Plate Wing to a Transverse Gust at Low Reynolds Numbers

Simon Corkery*, Holger Babinsky†

John Harvey‡

Department of Engineering, University of Cambridge, United Kingdom

In this article the unsteady response of a flat plate wing encountering a transverse gust is presented. The aim of this study is to understand how the lift and drag forces of a wing respond to a large amplitude wind gust of magnitude equivalent to the flight speed and at Reynolds numbers relevant to biological fliers and unmanned aerial vehicles. A gust rig capable of generating large amplitude top-hat shaped gust profiles was constructed in a towing tank to replicate the ideal 'sharp edge' Kussner gust. In addition, a new technique that enables vibration rejection from unsteady force measurements through improved kinematic measurements with inertial sensors is described. Measurements show that for a gust ratio of 1, a leading edge vortex forms on entry into the gust and vorticity is shed at the trailing edge in a planar manner. Large deformation of the gust shear layers is visible on wing entry, despite which linear theory is found to fit force measurements surprisingly well. Discernible differences, however, arise upon exit of the gust.

I. Introduction

The development of small low cost sensors and flight platforms has facilitated extensive growth in the use of unmanned aerial vehicles (UAVs) for military, commercial and consumer purpose. Applications include professional cinematography, surveillance and rapid transport of goods between geographical locations. While the small size of UAVs is beneficial from a cost and accessibility standpoint, herein lies a limitation from a flight stability and safety perspective. Small UAVs operate at altitudes well within the atmospheric boundary layer and fly across high shear and wake regions behind local obstructions.¹ In this region the wind turbulence intensity can exceed 50%.^{2,3} For a typical radio aircraft sized fixed wing UAV, rapid changes in incidence in excess of 25°, as well as span-wise variation in incidence of up to 15° causing roll instability have been measured.¹ Such extreme variations in incidence are compounded where reducing flight velocity leads to high gust ratios. Consequently it has been shown that for both biological fliers and man-made machines, the safe operating wind speed is significantly reduced with decreasing flight platform size.^{1,2,4-6}

Despite clear flight limitations of UAVs, existing research into the response of aerofoil lifting surfaces to wind gusts has historically been directed toward the application of manned flight, whether that be rotor or fixed wing aircraft. During forward flight of helicopter or tilt-rotor aircraft, tip vortices from the upstream blades is advected downstream and can interact with the following blades. Studies of this interaction are typically limited to small velocity perturbations and Reynolds numbers in excess of 200,000.⁷⁻¹¹ For such conditions the phenomenological based Kussner, Wagner, or Theodorsen models have been shown to fit measurements.¹²⁻¹⁶ Such theories are linear, assume small angles and describe the effect on bound circulation due to a vortex sheet advecting from the trailing edge at the free stream velocity.

Previous research on lift generation for aerofoils operating at low Reynolds numbers and undergoing highly unsteady '*surging*', '*pitching*' or '*plunging*' motions has shown that in contrast to the linear models, bound

*Ph.D., sjc276@cam.ac.uk.

†Professor, hb@eng.cam.ac.uk, AIAA Associate Fellow.

‡Professor, jkh28@cam.ac.uk, AIAA Associate Fellow.

circulation is small¹⁷ and vorticity is shed from the leading and trailing edges. This vorticity can amalgamate into leading and trailing edge vortices (LEV and TEV). Lift is generated through a combination of the change in impulse of the flow field due to growth and advection of the LEV and TEV, as well as due to classical added mass.¹⁸⁻²⁰ It is unknown whether the same lift production mechanisms occur when a wing progressively enters a large amplitude 'transverse' gust, the gust type that was shown to be problematic to UAV roll stability. This is due perhaps to the experimental challenges creating a transverse gust encounter entails. The primary aim of this paper is thus to present and characterise a transverse gust rig developed to replicate the 'ideal' high amplitude sharp edge gust. Particle Image Velocimetry (PIV), flow visualisation and force measurements are taken on a wing entering the transverse gust to identify discrepancies with the linear Kussner theory. A technique developed to quantify and reject vibration contamination from unsteady force measurements to improve accuracy is also presented. The Kussner model is discussed next.

A. Kussner's sharp edge gust model

The Kussner model describes the growth in lift coefficient for a flat plate wing gradually entering a sharp edged transverse gust as shown in figure 1. The model assumes the gust to be a non-deformable shear layer, thus allowing the wing to be modelled as a broken line aerofoil.²¹ The camber 'pivot' and angle of incidence progressively changes upon gust entry, which leads to changes in bound circulation. As circulation must be conserved, vorticity is shed into the wake at the trailing edge which delays growth in lift due to downwash induced back onto the aerofoil. The general lift coefficient is given by equation (1),

$$C_L = 2\pi \frac{V}{U} \psi(x/c), \quad (1)$$

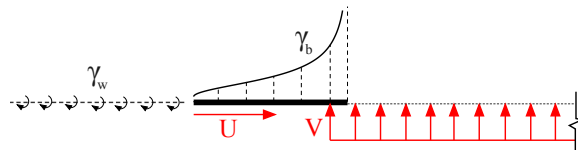


Figure 1: Schematic of Kussner's problem. Adapted from Leishman.²²

where $\psi(x/c)$ is the Kussner response function to a gust of magnitude equal to the free stream. An approximation for the Kussner function is given by Bisplinghoff et al.²³ (equation 2) and the corresponding change in lift coefficient is shown in figure 2 (solid line). The lift coefficient increases rapidly from zero as the leading edge enters the gust, attains approximately 70% of the steady state after 2 chord lengths.

$$\psi(x/c) = \frac{4(x/c)^2 + 2(x/c)}{4(x/c)^2 + 5.64(x/c) + 0.80} \quad (2)$$

While equation (2) describes the lift for a gust of unit magnitude and infinite extent, the response to any other arbitrary gust profile can be calculated by means of Duhamel's integral. The response is found by decomposing the input function into a series of impulses, for each of which a change in lift coefficient is calculated in accordance to equation 1. The total response is thus determined by linear superposition of the response of all past impulses. For a gust of two chord lengths this is shown by the dashed line in figure 2.

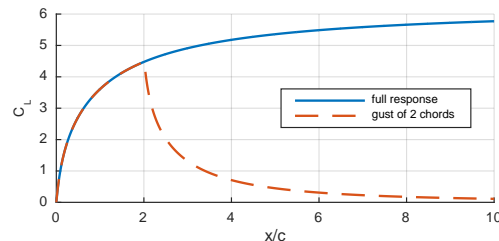


Figure 2: Indicial response function for a unit gust ($V/U = 1$)

II. Experimental setup

A specially designed gust apparatus was constructed to produce an ideal sharp edge gust in the Cambridge University Engineering Department (CUED) 9x1x1 metre towing tank. Water is used as the working fluid to take advantage of Reynolds number scaling effects, whereby flow speeds are lower and forces are approximately 4 times greater compared to the equivalent flow conditions in air. Particles can additionally be suspended in the fluid for particle image velocimetry and dye injected for flow visualisation. The test section of the tank has glass side walls and floor for optical access and is 2 metres in length. For the current experiments a water depth of 0.80 metres is used. All force and PIV measurements are averaged over 5 runs. The tank is left to settle for 15 minutes between each test run, after which turbulence has decayed to below the level quantifiable with the PIV system.²⁴ The design of the gust system is described next.

A. Gust rig

Conventional wind tunnel based gust rigs introduce transverse velocities by typically one of two means. One method uses a pair or cascade of actuated vanes upstream of the model to 'turn' the incoming flow.^{12, 25–30} However, this can be limited to deflection angles of $10 - 20^\circ$ due to flow separation on the vanes, coupling of the free stream velocity with vane deflection angle and increased turbulence levels. The second gust generation method involves 'jetting' flow at a fixed location and angle into the tunnel.³¹ This technique both fixes the cross wind angle and can require relatively complex mechanical shutter systems. Furthermore, the model experiences a uniform change in incidence and not the progressive gust entry shown in figure 1. Achieving a progressive gust entry with a jet in a wind tunnel would require an injection location that travels with the free stream. While this could be possible to construct, it is complex and unpractical.

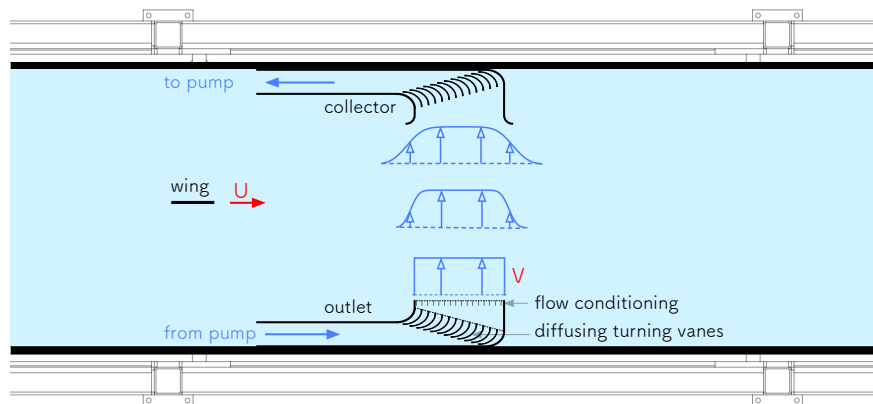


Figure 3: Schematic of the gust setup inside the tank. View from above the test section.

We make use of the CUED towing tank because unlike a wind tunnel, the flow field is directly representative of an aircraft or UAV in flight, i.e. the flow is stationary while the wing is translating. A transverse gust can thus be replicated by simply creating a velocity perturbation with a 'fixed' location in space, in an otherwise stationary fluid. The UAV, or flat plate wing in this case is attached to a carriage and is towed through the gust as it would if in real flight. A similar towing technique has been used for cross wind studies on lorry and railway vehicles, whereby the model is towed through the side of an open jet wind tunnel,³² as well as a jet in a water tank.³³ A schematic of the final design utilised for the following experiments is shown in figure 3. The system has three primary means of flow control. Firstly, the gust is introduced into the flow field using a pump system to enable independent control of the gust velocity relative to the wing. This is to enable practically any gust ratio (V/U) to be generated. Secondly, the pump ducting is used to 'condition' the gust into the desired velocity profile before entering the towing tank. Almost any gust profile can thus be created by the use of wire mesh 'resistance' screens, as opposed to being limited to just a self similar jet profile. Finally, the return circuit of the pump is used to 'collect' the gust, which minimises both turbulent mixing of the gust with the surrounding flow field and reduces recirculation of fluid in the tank. Keeping large scale turbulence to a minimum is essential to improve the quality and repeatability of measurements

taken during each test run. Recirculation in the tank is undesirable as it will take time for the gust system to reach steady state once started and the supposed quiescent regions either side of the gust will instead be dominated by a large vortical flow field.

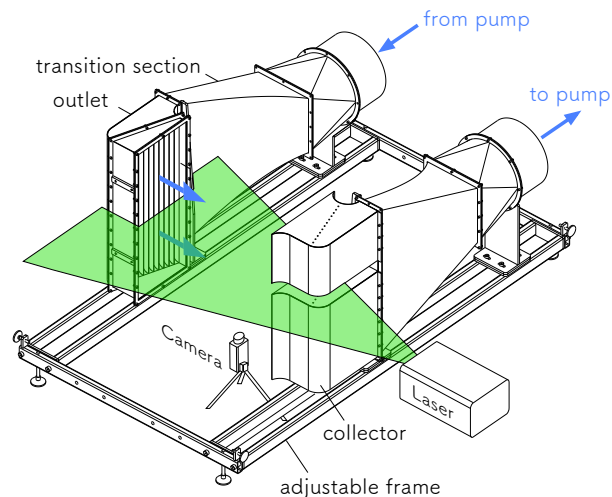


Figure 4: Gust ducting and PIV configuration.

Figure 4 shows the geometry and mounting configuration of the duct system. The outlet jet has a width of 240 mm and height of 600 mm. Flow is conditioned immediately prior to entry into the tank using a honeycomb (3.2 mm cell width) and a mesh screen to remove transverse and axial velocity perturbations. The pressure drop coefficient of the outlet screen is $K = 8.55$ for the design velocity of 0.5 m/s, where $K = \Delta P / \frac{1}{2} \rho U^2$. Based on a wing chord of 120 mm, the gust has a relative width of 2 chords. According to the Kussner function given prior in figure 2, the lift coefficient would reach approximately 70% of the steady state coefficient for a gust of infinite width by the point where the leading edge of the aerofoil reaches the 'back' gust shear layer.

The large geometry of the outlet (and thus the required collector) poses two problems. The confines of the towing tank walls requires flow to be redirected by 90° such that it can exit the outlet ducting in the direction transverse to the carriage path. Typical turning vanes are too large geometrically to fit the tank confines without introducing large blockage. The second problem is flow from the pumps must be diffused from the pump to outlet with an expansion ratio of 3, however, it is unpractical to include a large diffuser section. Flow separation must additionally be avoided as this will lead to non-uniformities and unsteadiness in the outlet velocity profile. To overcome both constraints a cascade of diffusing turning vanes was used. Without boundary layer control diffusing turning vanes have been shown to have total pressure losses similar to that of standard turning vanes without diffusing,³⁴ although the maximum expansion ratio tested is 1.45. The behaviour of a cascade of diffusing turning vanes with area ratio of 3 is thus unknown, but one might expect flow separation and unsteadiness. Boundary layer control is thus employed, similar to that of a wide angle diffuser where a wire mesh screen is located directly behind the vanes. According to the guidelines by Mehta and Bradshaw,³⁵ a pressure drop coefficient of at least $K = 2$ will suffice to ensure flow reattachment and uniformity of the outlet flow. Similar vanes are used on the gust collector, however, no boundary layer control is required as the flow is entering a gradual contraction. Both the outlet and collector pieces are connected to flexible hosing leading to the pump through constant area rectangle to circle transition sections. The system is driven using a 2.2 kW continuously variable speed axial flow pump, giving a velocity range from 0-0.50 m/s. The gust outlet and collector are mounted to an adjustable frame that allows the spacing of the outlet and collector to be varied between 240 to 600 mm in 120 mm increments. The model utilised here comprises a carbon fibre flat plate, with dimensions of 120 mm chord, 480 mm length and a 4 mm thickness. Based on wing chord (c) and free stream velocity (U), the setup gives a working Reynolds number range up to approximately 50,000, for which a maximum gust ratio of 1 is possible.

B. PIV

The setup of the PIV laser and camera system relative to the gust outlet is additionally shown in figure 4. A dual cavity Nd:YLF laser (527 nm) casts a light sheet horizontally through a gap in the collector module. This is setup to intersect the wing at the mid span location. A single Phantom Miro 310 camera is positioned underneath the tank and TiO_2 particles were photographed at a rate of 200 Hz. PIV frames were downsampled and processed at 100 Hz. Each frame was processed with deformable interrogation windows of nominal size 12x12 pixels with 50% overlap. The measurement error is approximately 3%, with more detailed description of error sources for the setup given by Corkery et al.²⁰

C. Force and inertial measurement systems

Lift and drag forces on the wing were measured using a 2 component 50 N force balance shown in figure 5. Cross talk between balance channels is less than 0.5% and the resolution of each channel is 0.01 N. The moment error due to offset loading of the wing relative to the balance sensors is less than 2%. The maximum error is therefore 2.5%. The balance is mounted directly to the tank carriage such that the balance sensors are in fixed alignment with the lift and drag directions, while the angle of incidence of the wing is adjusted relative to the balance. A 180 mm diameter end plate is located at the top wing tip, which is set flush into the skim plate which spans the width of the tank. The skim plate is attached rigidly to the carriage and suppresses surface wave effects in the vicinity of the wing. There is a 5 mm radial gap between the end and skim plates to circumvent the transmission of forces from the skim plate to the force balance. The arrangement produces a mirror image of the flow and wing, thus giving the wing an effective aspect ratio of 8. The design additionally avoids the requirement for a tip clearance gap between the wing and skim plate, which has been suspected of introducing three dimensional effects that are detrimental to span-wise coherence of the leading edge vortex.^{36,37} Embedded within the carbon wing is an ADXL335 3 component micro electromechanical accelerometer. Wiring runs internally through the wing for minimal flow disturbance. The sensor can measure accelerations up to ± 3 g, has a nonlinearity of less than $\pm 0.3\%$ and cross sensitivity of $\pm 1\%$. A second accelerometer is located on the towing tank carriage. The velocity and position of the carriage is calculated by numerically integrating the acceleration measured using the carriage mounted accelerometer. Gradual 'drift' in velocity and position due to cumulative sensor error is corrected by measuring the absolute position given by a separate quadrature linear encoder with 1 mm resolution. Combined position accuracy is estimated to be of order of 0.01 mm. Data is recorded using LabView and a National instruments 14 bit data acquisition card at a frequency of 5 kHz.

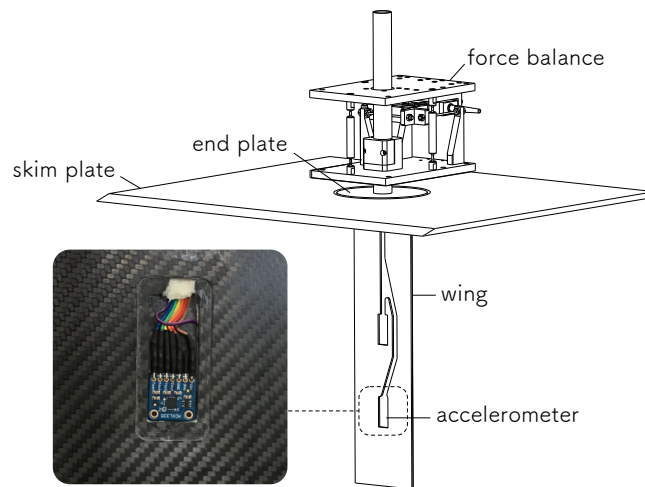


Figure 5: Wing and balance configuration.

III. Inertial force decomposition

Vibration due to flexibility of a load cell, sting or model can add significant noise to force measurements. This noise is particularly detrimental at low Reynolds numbers, whereby forces of interest can be just a fraction of a Newton. Filtering is often employed to smooth over vibrations,^{24,38-41} however, this distorts transient forces by reducing their peak and increasing bandwidth.⁴⁰ The necessity for filtering can therefore limit the usable frequency range of force measurements to below the lowest mode of vibration of the system. This is problematic for the relatively sharp edge gust experiment conducted here as frequency components of the transient fluctuations in force are above the natural frequency of the wing.

An additional source of measurement error results from the model and force balance self mass. During regions of carriage acceleration, an inertial force is applied through the load cell to accelerate the wing and balance mass. This force component is often quantified by taking the average of a series of 'tare' results from identical kinematic test runs conducted in air. The tare experiment takes advantage of the approximately 850 times difference in density between air and water, thus isolating the inertial component as fluid dynamic forces are comparatively negligible. This method is not, however, without fault. Direct subtraction of the inertial force from each 'wet' run introduces additional noise due to a mismatch in resonant frequencies between the dry and wet tests. The mismatch is a result of the increase in apparent mass of the model in water and subsequent reduction in natural frequency. Further error in kinematics can be introduced as the carriage actuator responds differently due to increased model loading. It is therefore desirable to improve the means which both model vibration and the self mass force are rejected.

In the following sections the equations of motion for the wing are derived to show that the use of accelerometer sensors enables inertial forces on the wing to be directly quantified. As model vibration and self mass are inertial forces, these can therefore be directly subtracted from the force measurements. This enables fluid dynamic derived force contributions to be isolated with increased resolution and accuracy.

A. General equations of motion

First we will consider the equations of motion for a flat plate wing undergoing arbitrary planar translation. As shown in figure 6, a wing coordinate frame $W_x - W_z$ is set at an arbitrary angle α to a global X-Y coordinate. The fluid is assumed to be stationary at infinite distance from the X-Y coordinate origin.

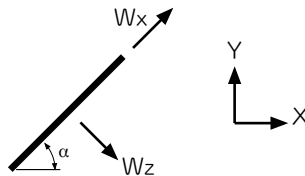


Figure 6: Coordinate systems.

In a viscous flow the inertial forces acting on a body can be deconstructed into two components. The first is attributed to body motion in an irrotational fluid and the second is due to vorticity in the flow field about the body.^{42,43} Acceleration of the wing in the direction perpendicular to its chord causes an added mass force, which is realised by a pressure difference across the plate surface. If the plate is assumed infinitely thin the added mass force must act perpendicular to the surface. For a flat plate wing with chord length c , length h , the mass component is equivalent to the mass of a cylindrical volume of fluid with a diameter of one chord ($m_{vt} = \rho h \frac{\pi c^2}{4}$). The force attributed to vorticity in the flow field is to be collected as one component F_{other} , which is typically the force of interest. The wing and balance system have mass m_w .

The force applied by the balance to the wing in the W_x and W_z directions is,

$$F_{wx} = m_w a_{wx} - F_{other,wx}, \quad (3)$$

$$F_{wz} = (m_w + m_{vt}) a_{wz} - F_{other,wz}, \quad (4)$$

where the subscripts wx and wz defines values in the Wx and Wz directions respectively. As shown in figure 7, the force measured by the load cell acts in an equal and opposite direction to that applied to the wing. Resolving the components of force on the balance in the X-Y coordinate frame gives equations (5) and (6). The terms $F_{other,X}$ and $F_{other,Y}$ are the transformed equivalent of $F_{other,wx}$ and $F_{other,wz}$:

$$F_{b,X} = -(m_w + m_{vt}) a_{wz} \sin \alpha - m_w a_{wx} \cos \alpha + F_{other,X} \quad (5)$$

$$F_{b,Y} = (m_w + m_{vt}) a_{wz} \cos \alpha - m_w a_{wx} \sin \alpha + F_{other,Y} \quad (6)$$

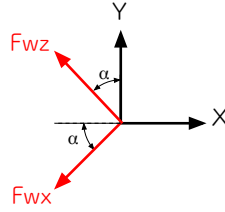


Figure 7: Forces the wing applies to the balance

For the experiments at hand the wing is constrained in the Y direction by the rails of the tank and therefore the wing can only experience accelerations in the X direction. The X direction acceleration, a_{car} , is directly measured with a carriage mounted accelerometer. Resolving a_{car} into the wing coordinate system gives:

$$a_{wx} = a_{car} \cos \alpha \quad (7)$$

$$a_{wz} = a_{car} \sin \alpha \quad (8)$$

Substituting equations (7) and (8) into (5) and (6) gives the forces applied to the force balance due to body motion and flow field vorticity.

$$F_{b,X} = -a_{car} (m_{vt} \sin^2 \alpha + m_w) + F_{other,X} \quad (9)$$

$$F_{b,Y} = m_{vt} a_{car} \sin \alpha \cos \alpha + F_{other,Y} \quad (10)$$

B. Modal vibration

Here we derive an additional force component due to structural vibration, or motion of the test model relative to the force balance. It is assumed that the body has only one mode of vibration in each of the Wx and Wz directions. We utilise the three axis accelerometer shown previously in figure 5 to measure the vibration modes. The acceleration due to vibration (a_v), is the difference between the carriage and wing accelerations.

$$a_{v,wx} = a_{wx} - a_{car} \cos \alpha \quad (11)$$

$$a_{v,wz} = a_{wz} - a_{car} \sin \alpha \quad (12)$$

Assuming only inertial effects are dominant, the force on the wing in the Wx and Wz directions due to wing vibration is:

$$F_{v,wx} = m_{vx} a_{v,wx} \quad (13)$$

$$F_{v,wz} = m_{vz} a_{v,wz} \quad (14)$$

The mass terms (m_{vx} and m_{vz}) are modal or effective masses as the entirety of the model will not experience the same accelerations as that measured with wing embedded accelerometer. It is important to note that the modal masses are a combination of both the wing and fluid added mass. These can be found through an initial calibration to be described in section D. Resolving the force on the balance into the X-Y directions gives the force on the balance due to vibration:

$$F_{v,X} = -m_{vz} \sin \alpha (a_{wz} - a_{car} \sin \alpha) - m_{vx} \cos \alpha (a_{wx} - a_{car} \cos \alpha) \quad (15)$$

$$F_{v,Y} = m_{vz} \cos \alpha (a_{wz} - a_{car} \sin \alpha) - m_{vx} \sin \alpha (a_{wx} - a_{car} \cos \alpha) \quad (16)$$

C. Combined force

The total force applied to the load cell is the sum of the mean acceleration and vibration components. Thus,

$$\begin{aligned} F_X &= F_{b,X} + F_{v,X} \\ &= -\underbrace{a_{car} m_{vt} \sin^2 \alpha}_{\text{virtual mass}} - \underbrace{a_{car} m_w}_{\text{self mass}} - \underbrace{m_{vz} \sin \alpha (a_{wz} - a_{car} \sin \alpha) - m_{vx} \cos \alpha (a_{wx} - a_{car} \cos \alpha)}_{\text{vibration}} + \underbrace{F_{other,X}}_{\text{remainder}}, \end{aligned} \quad (17)$$

$$\begin{aligned} F_Y &= F_{b,Y} + F_{v,Y} \\ &= \underbrace{m_{vt} a_{car} \sin \alpha \cos \alpha}_{\text{virtual mass}} + \underbrace{m_{vz} \cos \alpha (a_{wz} - a_{car} \sin \alpha) - m_{vx} \sin \alpha (a_{wx} - a_{car} \cos \alpha)}_{\text{vibration}} + \underbrace{F_{other,Y}}_{\text{remainder}}. \end{aligned} \quad (18)$$

Equations (17) and (18) show that through application of potential theory and select placement of inertial sensors, the measured force can be deconstructed into virtual mass, self mass and vibration components. The remaining component encompasses forces arising from vorticity in the flow field. As we are uninterested in force contributions due to the model self mass and vibration, we can simply subtract these components to leave the virtual mass and viscous forces of interest.

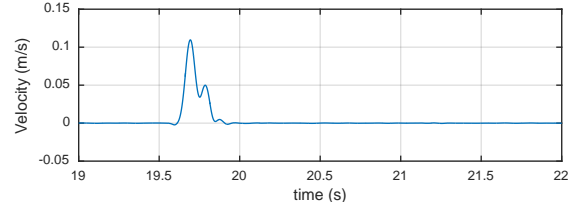
D. Calibration

The mass components m_w , m_{vt} , m_{vx} and m_{vz} can be readily found. Calibration of m_w was performed simply through turning the balance on the side such that the wing and balance self weight force due to gravity acts in the direction of the balance sensors ($m_w = \Delta F / \Delta a$). The virtual mass m_{vt} is calculated assuming the two dimensional potential flow solution, while the modal masses were found by setting the wing to an angle of incidence of 45° and subjecting the towing tank carriage to an impulse velocity profile while in water (change in displacement of 10 mm). An angle of 45° is used to induce free vibration in both the Wx and Wz directions. The velocity profile is shown in figure 8a and the deconstructed force response in the X, or negative drag direction is shown in figure 8b. After the impulse (from 20 seconds and onward) the tank carriage is at rest, $a_{car} = 0$ and the wing freely vibrates. Assuming non-bound vorticity in the flow field is negligible, the masses m_{vz} and m_{vx} are found by solving equations (13) and (14). Here the modal mass terms were averaged between the time of 20 to 21 seconds. Mass parameters from the calibration are given in table 1.

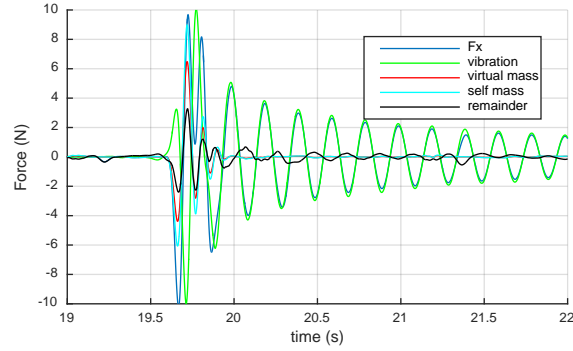
Table 1: Mass parameters (kg)

m_w	m_{vx}	m_{vz}	m_{vt}
3.75	1.54	3.70	5.43

During the free vibration region the force due to vibration (green line) inferred using the wing embedded accelerometer closely follows the transient force fluctuations measured using the balance (F_x , blue line). Subtraction of the vibration, virtual mass and self mass components from F_x leaves the remainder force contribution (black line). There is only minor variation in the remainder force during the entirety of the impulse experiment. As we expect inertial force contributions to be dominant during the calibration run, lack of variation in the remaining force contribution indicates that the decomposition model and experimental setup was successful in capturing the inertial force components. While some low pass filtering was still required to remove high frequency vibration and electrical noise, it was possible to increase the cut-off frequency to approximately 5 times the rig's first mode resonant frequency. In the following section the velocity profile from the gust rig is characterised.



(a) Velocity profile



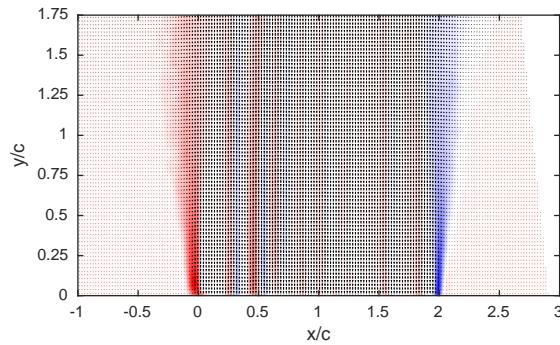
(b) X direction force component (-drag)

Figure 8: Calibration of inertial force system. A moving average with a period of 0.05 seconds is applied to smooth high frequency noise.

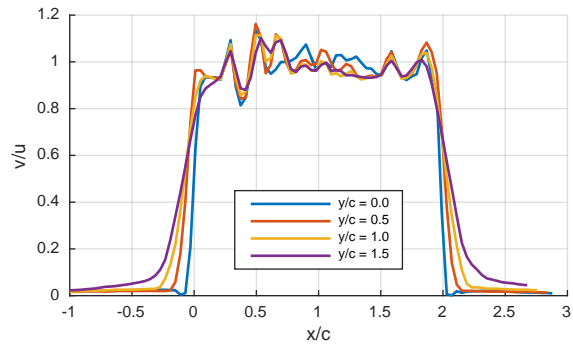
IV. Gust rig velocity profile

A. Steady state

A 10 second time average quiver plot of flow exiting the gust outlet during steady state operation is shown in figure 9a. Corresponding graphs of the velocity profiles are shown in figure 9b. A sharp edge or top-hat velocity profile is visible for $y/c = 0$, while the edges of the velocity profile spread due to the growth of the shear layer with increasing distance from the gust outlet. Diffusion of the shear layers either side of the gust is visible in figure 9a. The streaks of vorticity and corresponding fluctuations in the mean velocity profile inside the gust itself (from $s/c = 0$ to 2) are due to the wakes of the turning vanes upstream in the gust outlet (see figure 3). This is to be the subject of further investigation and development.



(a) Velocity quiver with contour of normalised vorticity



(b) Mean velocity profile

Figure 9: Flow velocity and normalised vorticity for of the gust sequentially averaged over 10 seconds.

B. Flow Unsteadiness

The unsteadiness of the cross flow region is quantified by the parameters $I_u = \frac{\sqrt{(u')^2}}{\bar{V}}$ and $I_v = \frac{\sqrt{(v')^2}}{\bar{V}}$, which is the ratio of the average u and v component perturbation velocities (u' and v' respectively) relative to the average gust velocity (\bar{V}). In figure 10, I_u and I_v are shown for 1000 consecutive PIV frames (10 seconds) taken once the gust has reached steady state. This parameter is analogous to a turbulence intensity, however, represents a spatial average due to the size of each PIV interrogation window.⁴⁴ For the present setup the side length of each processing interrogation window is 5.6 mm (4.6 % chord), thus turbulent eddies with smaller length scales are not resolved. Nonetheless, from figure 10 perturbations in the u and v velocities with a standard deviation of approximately 20% of the gust velocity are present within the shear layer along the gust edge at a distance of 1.5 chord lengths from the outlet. This appears to reduce closer toward the gust outlet. At the centreline of the gust the perturbations are typically between 2 and 3 %, which is similar to the 'undisturbed' regions outside the gust.

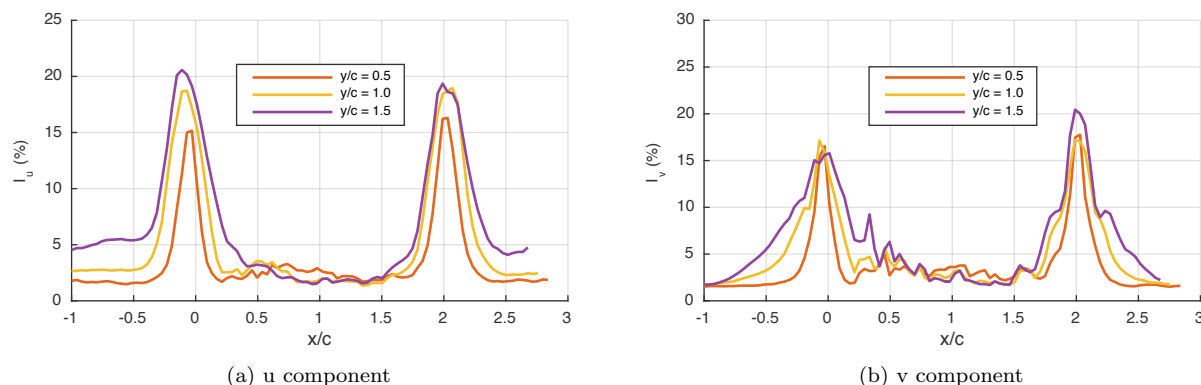


Figure 10: Flow unsteadiness as a percentage of the mean gust velocity (0.2 m/s).

V. Wing gust measurements

Flow visualisation, PIV and force measurements are taken for the flat plate wing entering the gust at offset of 1.5 chord lengths from the gust outlet. While reducing the distance between the gust outlet and wing increases both flow steadiness and the 'sharpness' of the gust edge, for these measurements a large offset distance is used to reduce blockage of the outlet on the flow field and thus minimise the possibility of changing the effect of the wing on the gust. The Reynolds number for flow visualisation was 5000, while this was increased to 20,000 for PIV and 40,000 for force measurements. Next the flow topology is considered, which is followed with a comparison of the lift force measurements with that predicted using the Kussner model.

A. Flow topology

Figure 11 shows flow features visualised by injecting a soy milk and methylated spirit dye mixture into the flow at both the leading edge of the flat plate wing and in the shear layers either side of the gust outlet. The dye mixture was selected as density can be varied to match the water in the tank by adjusting the milk/methylated spirit ratio. The dye was illuminated using the PIV laser which was defocussed to a nominal width of 40 mm to allow for illumination of all of the dye that may have drifted in the span-wise direction. PIV measurements showing gradual entry of the wing into the gust are shown in figure 12.

From figures 11 and 12 the following can be observed:

- Prior the the wing entering the gust the wing wake is visible as as a von Karman vortex street. The wing sheds positive vorticity from the upper boundary layer and negative vorticity from the lower.
- As the wing enters through the gust shear layer the von Karman vortex street is replaced with a Kelvin

Helmholtz type instability. The flow visualisation shows the vortices rotate in the clockwise direction, which is confirmed in the PIV measurements.

- A leading edge vortex of anticlockwise sign has formed above the surfaced of the wing. This is fed primarily by flow separating at the sharp leading edge of the aerofoil.
- The vortex appears to induce flow along the upper surface of the wing, in the direction tangential to the wing velocity. At $s/c = 1$ and onward secondary separation on the upper surface of the wing is visible. The secondary flow appears to be entrained into the leading edge vortex.
- As the wing enters the gust, the region of the left gust shear layer that is located below the wing is diverted toward the wing's trailing edge. The left gust shear layer located above the wing is shifted in the direction tangential to the wing path. The diversion of flow appears to be a result of the induced velocities from vorticity shed at the leading and trailing edges.

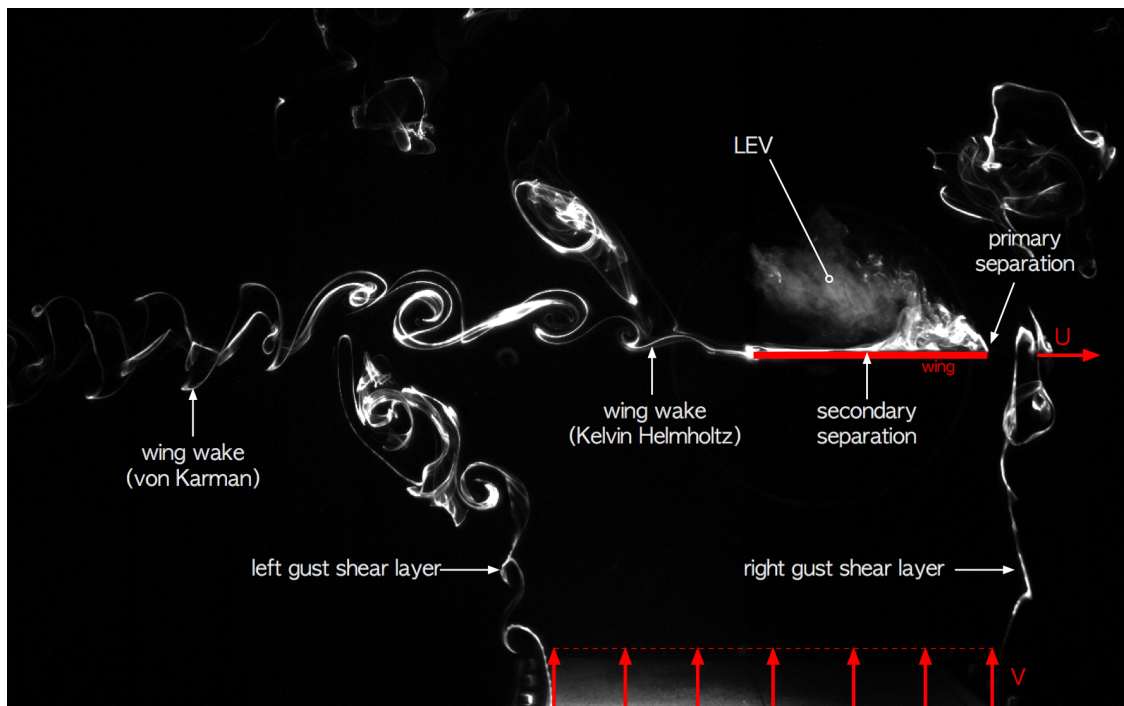


Figure 11: Streak lines showing gradual entry of a flat plate wing at 0 degrees incidence entering the shear layer of a sharp edge gust profile at $s/c = 2$. $Re = 5000$.

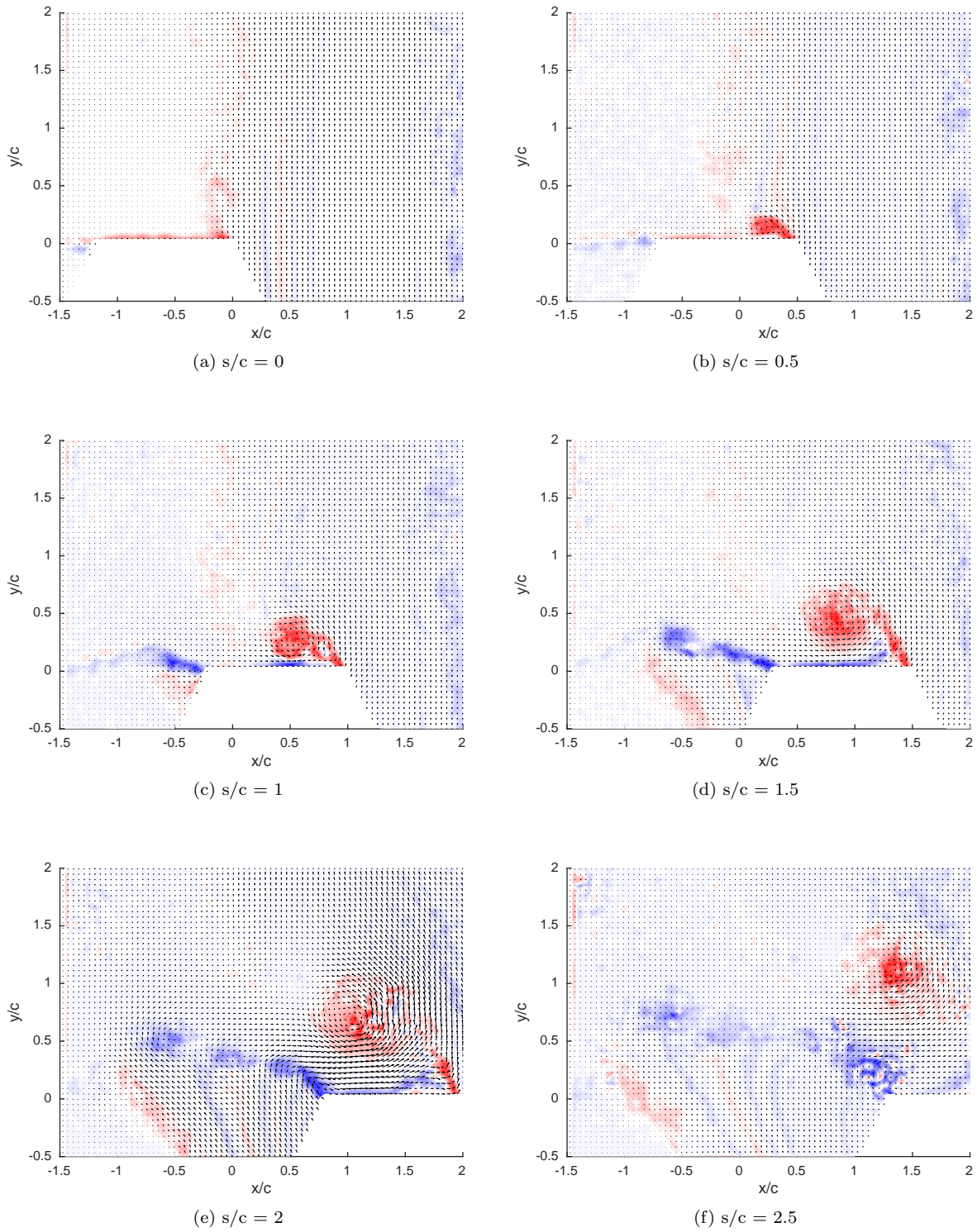


Figure 12: PIV measurement of flow field vorticity and velocity direction taken at $Re = 20,000$.

B. Force

Force measurement of the wing entering the cross flow region at an offset of 1.5 chord lengths from the gust outlet are shown in figure 13. The lift force coefficient (C_L) is defined here as the lift force normalised by the dynamic pressure based on the wing translation velocity U . It can be noted that the raw force measurement first rises prior to the nominal start of the gust. This is a result of the smearing of the mean gust velocity profile at the offset distance of 1.5 chord lengths described prior in section IV. The raw force measurement has been deconstructed into vibration and virtual mass components as given in the methodology section C. As the wing is travelling at constant velocity through the gust, there is no virtual mass component that can be attributed explicitly by measurement of wing acceleration ($a_{car} = 0$). Oscillations in the raw force measurement between 0 and 1 chord lengths can be attributed directly to wing vibration. Subtraction of the vibration and virtual mass force components to gives the remainder force component. This is the force component that can be attributed to that the gust applies to the wing and is thus the component of interest for comparison with the Kussner function.

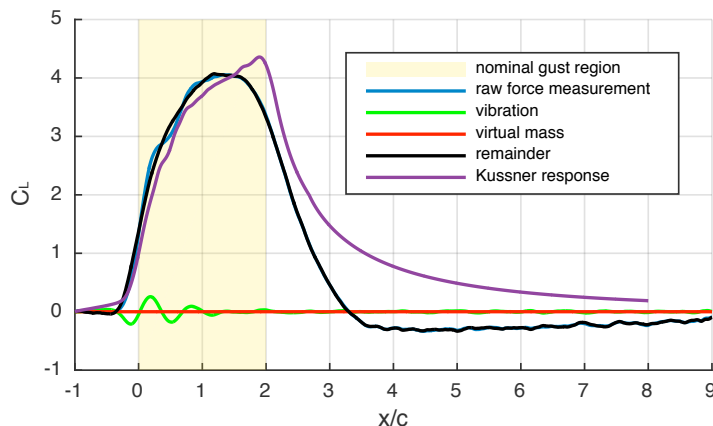


Figure 13: Decomposition of Lift coefficient with position into vibration and virtual mass components. The nominal gust region is indicated in yellow. $Re = 40k$.

The purple line on figure 13 is the Kussner response, which has been calculated for the mean gust profile at $y/c = 1.5$ through superposition of impulses. It should be noted that the Kussner function will be close to the ideal sharp edge response given in figure 2. The difference is attributed to discrepancies between the measured and ideal step velocity profiles. There is very surprising similarity (within $\approx 10\%$) between the Kussner response and force measurements for the entire extent of the gust region. Only on exit of the wing outside of the gust region do significant discrepancies between measurements and the Kussner response arise. The measured force overshoots $C_L = 0$ at $x/c = 3.25$ and curiously generates negative lift for $x/c > 3.25$. In contrast the Kussner response indicates positive lift which asymptotes toward zero with increasing wing distance.

VI. Conclusions

This paper presents a unique cross flow test rig that was developed specifically to measure the response of aerofoils to large amplitude transverse gusts. An inertial system was additionally developed to reduce the effect of vibration contamination from force measurements. PIV, flow visualisation and force measurements indicate:

- The cross flow system can generate a sharp edge jet into the towing tank with only minor disturbance to the surrounding fluid.
- Measurements of the velocity profile show reasonable uniformity. Minor variations in the cross flow velocity profile are present due to turning vane wakes, which is an issue to be addressed.
- The velocity profile is shown to be steady, albeit fine scale turbulence is yet to be quantified.

- The inertial force decomposition technique has been shown to allow the unsteady response of a model to be measured and compensated for frequencies up to 5 times that of the model's first mode of vibration.
- Entry of the wing into the gust region results in the formation of a large leading edge vortex and vorticity to be shed at the trailing edge.
- The trailing edge vorticity remains relatively planar, which fits the assumptions of a planar wake in the Kussner theory.
- The gust shear layers are deflected upon wing entry.
- Despite difference between the physical and modelled flow fields, the Kussner model fits surprisingly well with measurements of a flat plate wing in a sharp edge gust. Significant discrepancies only appear to be quantifiable upon exit of the gust.

Acknowledgments

The author would like to acknowledge the Cambridge Commonwealth European and International Trust, Churchill College and Schlumberger Limited for providing financial support.

References

- ¹Watkins, S., Milbank, J., Loxton, B. J., and Melbourne, W. H., "Atmospheric Winds and Their Implications for Microair Vehicles," *AIAA Journal*, Vol. 44, No. 11, nov 2006, pp. 2591–2600.
- ²Mohamed, A., Abdulrahim, M., Watkins, S., and Clothier, R., "Development and Flight Testing of a Turbulence Mitigation System for Micro Air Vehicles," *Journal of Field Robotics*, 2015.
- ³Walshe, D. E. J., *Wind-excited oscillation of structures*, H.M. Stationery Office, 1972.
- ⁴Watkins, S., Thompson, M., Loxton, B., and Abdulrahim, M., "On Low Altitude Flight Through the Atmospheric Boundary Layer," *International Journal of Micro Air Vehicles*, Vol. 2, No. 2, 2010, pp. 55–68.
- ⁵Spedding, G. R. and Lissaman, P. B. S., "Technical Aspects of Microscale Flight Systems," *Journal of Avian Biology*, Vol. 29, No. 4, 1998, pp. 458–468.
- ⁶White, C., Lim, E., Watkins, S., Mohamed, A., and Thompson, M., "A feasibility study of micro air vehicles soaring tall buildings," *Journal of Wind Engineering and Industrial Aerodynamics*, Vol. 103, 2012, pp. 41–49.
- ⁷Zanotti, A., Ermacora, M., Campanardi, G., and Gibertini, G., "Stereo particle image velocimetry measurements of perpendicular blade-vortex interaction over an oscillating airfoil," *Experiments in Fluids*, Vol. 55, No. 9, 2014, pp. 1–13.
- ⁸Peng, D. and Gregory, J. W., "Vortex dynamics during blade-vortex interactions," *Physics of Fluids*, Vol. 27, No. 5, 2015, pp. 1–23.
- ⁹Rival, D., Manejev, R., and Tropea, C., "Measurement of parallel blade-vortex interaction at low Reynolds numbers," *Experiments in Fluids*, Vol. 49, No. 1, 2010, pp. 89–99.
- ¹⁰Homer, M. B., Saliveros, E., Kokkalis, A., and Galbraith, R. A. M., "Results from a set of low speed blade-vortex interaction experiments," *Experiments in Fluids: Experimental Methods and their Applications to Fluid Flow*, Vol. 14, No. 5, 1993, pp. 341–352.
- ¹¹Mai, H., Neumann, J., and Hennings, H., "Gust response: a validation experiment and preliminary numerical simulations," *15th International Forum on Aeroelasticity and Structural Dynamics*, 2011, pp. 1–20.
- ¹²Patel, M. H., "Aerodynamic Forces on Finite Wings in Oblique Gusts," *Journal of Aircraft*, Vol. 19, No. 1, 1982.
- ¹³Patel, M. H., "Aerodynamic Forces on Finite Wings in Oscillatory Flow: An Experimental Study," *AIAA Journal*, Vol. 16, No. 11, 1978, pp. 1175–1180.
- ¹⁴Zaide, A. and Raveh, D. E., "Numerical Simulation and Reduced-Order Modeling of Airfoil Gust Response," *AIAA Journal*, Vol. 44, No. 8, 2006, pp. 1826–1834.
- ¹⁵Leishman, J. G., "Subsonic unsteady aerodynamics caused by gusts using the indicial method," *Journal of Aircraft*, Vol. 33, No. 5, 1996, pp. 869–879.
- ¹⁶Leishman, J. G., "Unsteady Aerodynamics of Airfoils Encountering Traveling Gusts and Vortices," *Journal of Aircraft*, Vol. 34, No. 6, 1997, pp. 719–729.
- ¹⁷Pitt Ford, C. W. and Babinsky, H., "Lift and the leading-edge vortex," *Journal of Fluid Mechanics*, Vol. 720, 2013, pp. 280–313.
- ¹⁸Stevens, P. R. R. J. and Babinsky, H., "Experiments to investigate lift production mechanisms on pitching flat plates," *Experiments in Fluids*, Vol. 58, No. 1, 2017, pp. 7.
- ¹⁹Babinsky, H., Stevens, P. R. R. J., Jones, A. R., Bernal, L. P., and Ol, M. V., "Low Order Modelling of Lift Forces for Unsteady Pitching and Surging Wings," *54th AIAA Aerospace Sciences Meeting*, jan 2016, pp. 1–12.
- ²⁰Corkery, S. J., Stevens, P. R. R. J., and Babinsky, H., "Low Reynolds Number Surge Response of a Flat Plate Wing at 90 Degrees Incidence," *AIAA SciTech Forum - 55th AIAA Aerospace Sciences Meeting*, 2017, pp. 1–16.
- ²¹Von Karman, T. and Sears, W. R., "Airfoil Theory for Non-Uniform Motion," *Journal of the Aeronautical Sciences*, Vol. 5, No. 10, 1938, pp. 379–390.

- ²²Leishman, J. G., *Principles of helicopter aerodynamics*, Vol. 18 of *Cambridge aerospace series*, Cambridge University Press, Cambridge, 2nd ed., 2000.
- ²³Bisplinghoff, R. L., Ashley, H., and Halfman, R. L., *Aeroelasticity*, Addison-Wesley series in mechanics, Addison-Wesley, Cambridge, MA, 1955.
- ²⁴Jones, A. R. and Babinsky, H., “Reynolds number effects on leading edge vortex development on a waving wing,” *Experiments in Fluids*, Vol. 51, No. 1, 2011, pp. 197–210.
- ²⁵Tang, D. and Dowell, E. H., “Aeroelastic Airfoil with Free Play at Angle of Attack with Gust Excitation,” *AIAA Journal*, Vol. 48, No. 2, feb 2010, pp. 427–442.
- ²⁶Saddington, A., Finnis, M., and Knowles, K., “The characterisation of a gust generator for aerodynamic testing,” *Proceedings of the Institution of Mechanical Engineers, Part G: Journal of Aerospace Engineering*, Vol. 229, No. 7, sep 2014, pp. 1214–1225.
- ²⁷Brion, V., Lepage, A., Amosse, Y., Soulevant, D., Senecat, P., Abart, J. C., and Paillart, P., “Generation of vertical gusts in a transonic wind tunnel,” *Experiments in Fluids*, Vol. 56, No. 145, 2015, pp. 1–16.
- ²⁸Patel, M. H. and Hancock, G. J., “A Gust Tunnel Facility,” Tech. Rep. 3802, Aeronautical Research Council, 1977.
- ²⁹Tang, D. M., Cizmas, P. G. A., and Dowell, E. H., “Experiments and analysis for a gust generator in a wind tunnel,” *Journal of Aircraft*, Vol. 33, No. 1, 1996, pp. 139–148.
- ³⁰Ham, N. D., Bauer, P. H., and Lawrence, T. L., “Wind tunnel generation of sinusoidal lateral and longitudinal gusts by circulation of twin parallel airfoils. Report CR-137547.” Tech. rep., NASA, 1974.
- ³¹Volpe, R., Da Silva, A., Ferrand, V., and Le Moynes, L., “Experimental and Numerical Validation of a Wind Gust Facility,” *Journal of Fluids Engineering*, Vol. 135, No. 1, 2013.
- ³²Humphreys, N. D., *High Cross Wind Gust Loads on Ground from Moving Model Experiments*, Ph.D. thesis, University of Nottingham, 1995.
- ³³Perrotta, G. M. and Jones, A. R., “Transient aerodynamics of large transverse gusts and geometrically similar maneuvers,” *54th AIAA Aerospace Sciences Meeting*, AIAA SciTech Forum, jan 2016.
- ³⁴Friedman, D. and Westphal, W. R., “Experimental Investigation of a 90 degree Cascade Diffusing Bend with an Area Ratio of 1.45:1 and with Several Inlet Boundary Layers. TN 2668,” Tech. rep., NACA, 1952.
- ³⁵Mehta, R. D. and Bradshaw, P., “Design Rules for Small Low Speed Wind Tunnels,” *The Aeronautical Journal of the Royal Aeronautical Society*, 1979, pp. 443–449.
- ³⁶Ol, M. and Babinsky, H., “Extensions of Fundamental Flow Physics to Practical MAV Aerodynamics: TR-AVT-202,” Tech. rep., North Atlantic Treaty Organization, 2016.
- ³⁷Son, O., Cetiner, O., Stevens, P. R. R. J., Babinsky, H., Manar, F., Mancini, P., Jones, A. R., Ol, M. V., and Gozukara, A. C., “Parametric Variations in Aspect Ratio, Leading Edge and Planform Shapes for the Rectilinear Pitch Cases of AVT-202,” *54th AIAA Aerospace Sciences Meeting*, 2016, pp. 1–17.
- ³⁸Granlund, K., Ol, M., and Bernal, L., “Experiments on pitching plates: force and flowfield measurements at low Reynolds Numbers,” *AIAA Paper*, Vol. 872, No. January, 2011, pp. 2011.
- ³⁹Jones, A. R. and Babinsky, H., “Unsteady Lift Generation on Rotating Wings at Low Reynolds Numbers,” *Journal of Aircraft*, Vol. 47, No. 3, 2010, pp. 1013–1021.
- ⁴⁰Pitt Ford, C. W., *Unsteady aerodynamic forces on accelerating wings at low Reynolds numbers.*, Ph.D. thesis, The University of Cambridge, 2013.
- ⁴¹Stevens, P. R. R. J., *Unsteady Low Reynolds Number Aerodynamic Forces*, Ph.D. thesis, The University of Cambridge, 2013.
- ⁴²Eldredge, J. D., “A Reconciliation of Viscous and Inviscid Approaches to Computing Locomotion of Deforming Bodies,” *Experimental Mechanics*, Vol. 50, No. 9, 2010, pp. 1349–1353.
- ⁴³Graham, W. R., Pitt Ford, C. W., and Babinsky, H., “An impulse-based approach to estimating forces in unsteady flow,” *Journal of Fluid Mechanics*, Vol. 815, 2017, pp. 60–76.
- ⁴⁴Westerweel, J., “Fundamentals of digital particle image velocimetry,” *Measurement Science and Technology*, Vol. 8, No. 12, 1999, pp. 1379–1392.